ADVANCED MATERIALS
www.advmat.de

Mechanostimulatory Platform for Improved CAR T Cell Immunotherapy

Abed Al-Kader Yassin, Carlos Ureña Martin, Guillaume Le Saux, Ashish Pandey, Sivan Tzadka, Esti Toledo, Jatin Jawhir Pandit, Tomer Sherf, Idan Nusbaum, Baisali Bhattachrya, Rajashri Banerji, Yariv Greenshpan, Muhammad Abu Abu Ahmad, Olga Radinsky, Menachem Sklartz, Roi Gazit, Moshe Elkabets, Saba Ghassemi, Ofir Cohen, Mark Schvartzman, and Angel Porgador**

Chimeric Antigen Receptor T (CAR T) cell immunotherapy has revolutionized cancer treatment, yet it is hindered by rapid T-cell exhaustion caused by uncontrolled activation during CAR generation. Leveraging insights into T-cell mechanosensing, a novel mechanostimulatory platform is engineered for T-cell activation based on an antigen-carrying surface with controlled elasticity and nanotopography. The platform is designed to optimize and balance T-cell exhaustion, proliferation, and CAR expression. It enhances the differentiation of T cells into the central memory subset, which is crucial for the persistence of CAR T cell therapy's anticancer effects. The platform produces CAR T cells with higher antitumor efficacy, as validated through ex vivo experiments, and with higher in vivo persistence and ability to suppress tumor proliferation, as compared to CAR T cells generated by standard protocols. RNA-seq analysis confirmed an increased transcriptional signature of central memory T cells. Furthermore, this platform completely eliminates T-cell toxicity associated with the non-viral transfection process typically observed with standard activation methods. This platform presents a promising pathway for improving the efficiency and safety of CAR T cell therapy.

1. Introduction

T cells expressing chimeric antigen receptors (CARs) have revolutionized cancer treatment through adoptive cellular immunotherapy.[1,2] Since the approval of Novartis' *Kymriah*™ in 2017, several other CAR T-cell therapies have received FDA approval, offering unprecedented therapeutic benefits for various hematologic malignancies. Currently, according to *clinicaltrials.gov*, over a thousand ongoing clinical trials are focused on improving CAR T-cell therapy and expanding its application to solid tumors. In the standard CAR T-cell generation process, primary T cells are isolated from a patient's peripheral blood, activated, genetically modified using a viral vector to express CARs, and expanded before adoptive transfer. However, prolonged ex vivo culture is associated with terminal differentiation and a loss

A. A.-K. Yassin, B. Bhattachrya, R. Banerji, Y. Greenshpan, M. A. Abu Ahmad, O. Radinsky, M. Sklartz, R. Gazit, M. Elkabets, O. Cohen, A. Porgador
The Shraga Segal Department of Microbiology Immunology, and Genetics
Faculty of Health Sciences
Ben-Gurion University of the Negev
Beer-Sheva 8410501, Israel
E-mail: angel@bgu.ac.il

C. Ureña Martin, G. Le Saux, A. Pandey, S. Tzadka, E. Toledo, J. J. Pandit, T. Sherf, I. Nusbaum, M. Schvartzman
Department of Materials Engineering
Faculty of Engineering
Ben-Gurion University of the Negev
Beer-Sheva 8410501, Israel
E-mail: marksc@bgu.ac.il

C. Ureña Martin, G. Le Saux, A. Pandey, S. Tzadka, E. Toledo, J. J. Pandit, T. Sherf, I. Nusbaum, M. Schvartzman
Ilse Katz Institute for the Nanoscale Science and Technology
Beer-Sheva, Israel

S. Ghassemi
Center for Cellular Immunotherapies
Perelman School of Medicine
University of Pennsylvania
Philadelphia, PA, USA

O. Cohen
Department of Software and Information System Engineering
Ben-Gurion University of the Negev
Beer-Sheva 8410501, Israel

The ORCID identification number(s) for the author(s) of this article can be found under https://doi.org/10.1002/adma.202412482

DOI: 10.1002/adma.202412482

of anti-tumor potency.[3] Eliminating the activation and proliferation phase enhances CAR T-cell anti-tumor potency but reduces CAR transduction efficiency.[4] Developing an optimized CAR T-cell production process that balances proliferation and anti-tumor function remains a key challenge in CAR T-cell immunotherapy.

In ex vivo settings, T cells are activated through the engagement of the T cell receptor (TCR)-CD3 complex and costimulatory CD28 receptors. While soluble antibodies targeting these receptors can initiate T-cell activation, a complete immune response is only achieved when the antibodies are tethered to a supporting surface—mimicking the way activating ligands are presented on the membranes of antigen-presenting or target cells in vivo. This tethering establishes the physical conditions necessary for T-cell activation, which involves the spatial exclusion of large phosphatase molecules from regions where clustered receptors are bound,[5] as well as conformational changes in the bound receptors.[6] In both clinical and research settings, antibody-coated magnetic microbeads are commonly used as T-cell activation surfaces. However, these beads were originally designed for unrelated applications, such as cell separation, and therefore lack key features essential for optimal and controlled T-cell activation.

One crucial feature is the elasticity of the ligand-carrying surface. Although the mechanism of T-cell mechanosensing remains an area of extensive research,[7] it is well established that T cells mechanically probe their environment, adjusting their response based on the stiffness of target cells in vivo and ligand-carrying surfaces ex vivo.[8–11] Another critical factor is the morphology of the activating surface. In vivo, the physiological T cell-target interface forms a complex 3D microstructure, which promotes the development of protrusions with receptor-rich sensing tips while segregating them from large phosphatase molecules.[12–14] 3D-microstructured surfaces have been shown to facilitate T-cell activation ex vivo—even in the absence of activating antibodies—by inducing artificial TCR-phosphatase separation.[15] Recognizing the growing importance of environmental elasticity and microstructure as physical regulators of T-cell activation, efforts have been made to develop a new family of materials for ex vivo T-cell activation.[16–19] However, these materials have primarily been shown to facilitate basic cell functions such as activation and proliferation.[10,11,20] In contrast, the potential for leveraging the elasticity and microtopography of the activating surface to enhance CAR T-cell immunotherapy remains largely unexplored.

In this study, we demonstrate that the strategic combination of a rationally designed microstructure and elasticity on T-cell activating surfaces significantly enhances the production and anti-tumor potency of CAR T cells (**Figure 1a**). To achieve this, we systematically investigated the impact of various elasticities and microstructural geometric parameters on key T-cell functions involved in the immunotherapeutic cycle, including activation, exhaustion, proliferation, and CAR transduction efficiency. These features are crucial components in the life cycle of CAR T cells and are essential for optimizing their production.[21] Using multivariate analysis, we identified the optimal set of physical parameters for activating surface design. When integrated into the standard T-cell production protocol, these surfaces promoted greater differentiation of CAR T cells toward a central memory phenotype compared to the standard method. As a result, CAR T cells produced using these surfaces exhibited superior antitumor efficacy, as validated through multiple assays, including in vitro lysis and ex vivo patient-derived xenograft (PDX) models. Additionally, their efficacy was confirmed through in vivo cancer-killing experiments in murine models, in which significantly reduced tumor proliferation and significantly enhanced CAR T-cell persistence in blood were manifested. Furthermore, we demonstrated that T-cell activation on these engineered surfaces enhanced the transcriptional signature associated with the central memory T-cell phenotype, which is critical for effective antitumor activity. These findings introduce a novel material-based approach for generating CAR T cells with superior anti-important efficacy compared to those produced using existing clinical methods.

2. Results

3. 3D Microtopography and Elasticity Cumulatively Regulate T Cell Activation, Exhaustion, CAR Transduction Efficacy, and Proliferation

To activate T cells using 3D microtopography, we employed a micro-/nano-pillar design previously utilized in fundamental mechanobiology studies,[22–24] including T-cell mechanobiology.[25] Figure 1a illustrates the general scheme of CAR T-cell activation and production using micro-/nano-pillar surfaces. Figure 1b and Figure S1 (Supporting Information) provide SEM and confocal images, respectively, showing T cells interacting with a functionalized micropillar platform. Our initial design featured various micro-/nano-pillar arrays. Specifically, we tested combinations of two diameters (500 and 1 µm) and aspect ratios (4 and 8), with a periodicity four times the pillar diameter (Figure 1c). These structures were fabricated through double replication of polydimethylsiloxane (PDMS) from a nanofabricated master mold (see Experimental Section). The resulting pillars were produced in three sets with bulk PDMS moduli of 0.5, 1.5, and 5 MPa. Hereinafter, surface structures with micropillars are denoted as x (diameter, µm) – y (aspect ratio) – z (elasticity, MPa) (Figure 1c). To engage activating and costimulatory receptors, the pillars were coated with a mixture of human anti-CD3 and anti-CD28 molecules. Control experiments utilized anti-CD3/CD28-coated magnetic beads (*Dynabeads*™) at a 1:1 bead-to-cell ratio, as well as flat PDMS surfaces of varying stiffness—both uncoated and anti-CD3/CD28-coated.

In the initial phase, we investigated how surface elasticity and topography influence T-cell functions critical for CAR T-cell production and subsequent antitumor efficacy. We isolated peripheral blood mononuclear cells (PBMCs) from three independent healthy donors and followed a standard CAR T-cell production protocol (Figure 1d). This process included 24 h of activation, 48 h of lentiviral transduction with CAR targeting human epidermal growth factor receptor 2 (HER2)—a marker expressed by breast and ovarian cancer cells—and four days of proliferation. Our goal was to identify the optimal combination of surface properties for achieving favorable outcomes. We evaluated 10 different parameters, including activation levels, assessed by CD69 and CD107 markers immediately after activation (day 1), transduction efficiency and proliferation, measured both immediately after transduction (day 3) and on day 7, and T-cell

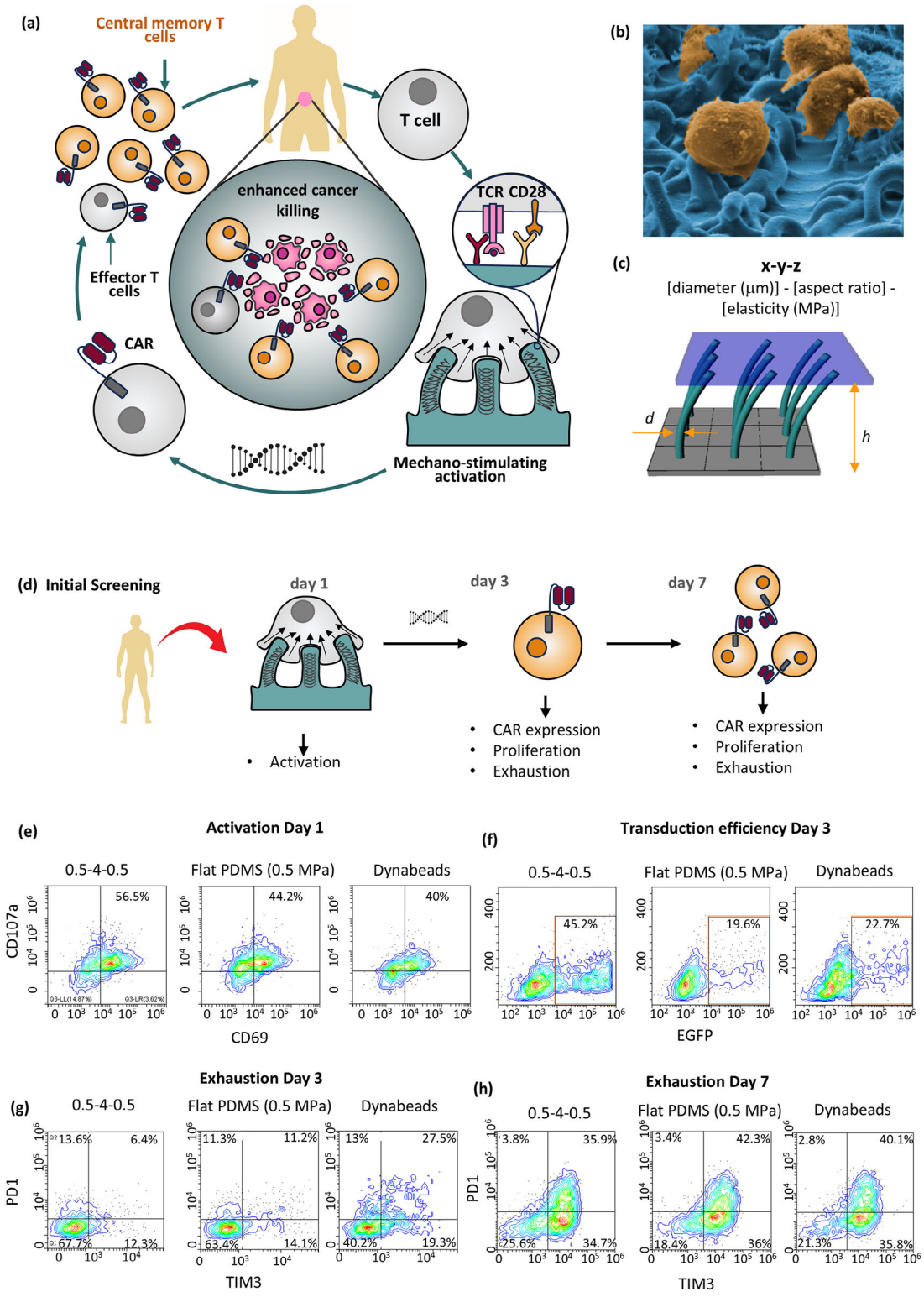

Figure 1. a) Schematic of CAR T cell generation workflow including activation with antibody-coated elastic microtopography. b) Representative scanning electron microscopy image of T cells on elastic microbrushes. c) Activation surfaces diagram with the experimental parameters highlighted: length (h), diameter (d), and effective stiffness calculation. d) Experimental setup and measurement points: day 1 activation, day 3 and 7 readout of CAR expression, activation, and exhaustion markers with Flow Cytometry (FC), as well as proliferation counting. e–h) FC of 0.5 (diameter, μm) – 4 (aspect ratio) – 0.5 (elasticity, Mpa), flat sample of same bulk stiffness and standard Dynabeads activation protocol where the percentage of double-positive for CD107a and CD69 on day one is shown as activation criteria (e), percentage of CD69 positive cells expressing CAR by eGFP reporter at day 3 (f) and double positive cells expressing PD1 and TIM3 as exhaustion read out at day 3 (g) and day 7 (h).

exhaustion, assessed by Programmed cell death protein 1 (PD1 and T cell Ig- and mucin-domain-containing molecule-3 (TIM3) markers on days 3 and 7. To measure transduction efficiency, we linked Enhanced Green Fluorescent Protein (eGFP) to the CAR gene via T2A, ensuring that membrane-associated CAR expression correlated directly with eGFP expression in a 1:1 ratio (Figure S2, Supporting Information).

In assessing T cell activation, both surface elasticity and topography exhibit notable effects on the assessed outcomes. Figure 1e–h and Figure S3 (Supporting Information) show representative raw flow cytometry data for selected donors and selected tested surfaces. In Figure 1e, T cells from a specific donor display enhanced activation when stimulated by elastic microtopography compared to the flat and rigid surface of Dynabeads. This positive impact of elasticity on activation aligns with the biphasic mechanosensitivity trend of T cells,[11,26] where activation increases with decreasing surface elasticity of antibody-bearing surfaces, particularly in the high megapascal range and beyond. Additionally, topography significantly influences activation, demonstrated by comparing T cells stimulated on pillars with those on flat PDMS surfaces of identical bulk modulus (Figure 1e). Furthermore, topography also significantly affects transduction efficiency and other functional responses such as exhaustion, as observed across various geometries (Figure 1f,g,h).

Comparing all tested activation surfaces is inherently complex due to the multiplicity of assessed outcomes, all of which must be considered alongside donor variability in T-cell responses. To address this complexity, we applied multivariate analysis. First, for each outcome, we aggregated measurements across donors and replicates and calculated a Z-score to normalize the data. Specifically, to account for donor variability (D1, D2, D3), we subtracted the mean value of all replicate measurements of *Dynabeads*™ for each donor (setting the *Dynabeads*™ mean performance to zero). The outcomes were then scaled by dividing by the standard deviation of the measurements across all surfaces for each outcome. This approach allowed us to rank the activation surfaces—12 topographical surfaces, three flat surfaces, three negative controls (without antibodies), and *Dynabeads*™ as a reference—based on their median performance across donors and replicates. Figures S4–S9 (Supporting Information) show the rankings for each outcome and the corresponding raw data per outcome and donor, while Tables S1 and S2 (Supporting Information) provide statistical details of the raw data. Next, we assessed the global performance of the 16 tested surface topologies (12 topographical surfaces, three flat surfaces, and *Dynabeads*™ as a reference) using a non-parametric ranking method to aggregate the multidimensional feature scores (see Extended Methods in the Supporting Information).

This analysis accounted for performance across all outcomes and enabled the ranking of the surfaces based on their outcome-specific performance (**Figures 2**, and S10, Supporting Information). Based on this analysis, we identified the highest-scoring surface, "0.5-4-0.5," as the optimized surface for T-cell activation, which was subsequently used in all further experiments (Figure 2). To visualize similarities and differences among the 16 topographies, we reduced the ten features into 2D maps (Figure S11, Supporting Information). Notably, in the ranking, we assigned equal weight to all outcomes, totaling ten: two outcomes reflecting proliferation efficacy (days 3 and 7), two for transduction efficacy (days 3 and 7), one for activation (day 1), and four for exhaustion (days 3 and 7). Activation influences both production efficacy, by enhancing transduction efficacy, and therapeutic efficacy. On the other hand, recent research highlights the critical role of exhaustion in the therapeutic efficacy of CAR,[27] which is why we considered four exhaustion-related outcomes out of the total ten. Even when considering only four equally weighted outcomes—activation, transduction, proliferation, and exhaustion (each representing the averaged relevant data)—we still identified surface 0.5-4-0.5 as the best-performing one (Figure S12, Supporting Information).

4. 3D Elastic Microstructure Enhances Differentiation into the Central Memory Type CAR-T Cells

Beyond refining the CAR T-cell production process, there is limited knowledge about the optimal composition of CAR T cells for adoptive immunotherapy. Several independent studies in murine models suggest that central memory T (T_{CM}) cell subsets exhibit enhanced antitumor functionality upon adoptive transfer and that a higher proportion of central memory-type T cells within CAR T-cell products is associated with greater antitumor efficacy.[28–31] A comprehensive analysis of human T-cell subsets in CAR T cells demonstrated that central memory (T_{CM}) cells, characterized by co-expression of C-C chemokine receptor type 7 (CCR7) and CD45RO, possess distinct engraftment capacities and improved function following adoptive transfer in preclinical trials.[32] Strategies to enhance CAR T-cell efficacy have been associated with an increased central memory phenotype. For example, IL-9-expressing human CAR T cells exhibited an enhanced central memory phenotype and improved antitumor efficacy.[33] Similarly, Tet methylcytosine dioxygenase 2 (TET2 disruption in CAR T cells derived from chronic lymphocytic leukemia (CLL) patients led to a greater central memory phenotype and higher antitumor potency.[34] Further research revealed that TOX high mobility group box family member 2 (TOX2) coordinates with TET2 to regulate central memory differentiation and enhance CAR T-cell efficacy in humans.[35] Additionally, a study examining the genomic and phenotypic characteristics of CAR T cells found that cells from patients in complete remission exhibited upregulation of genes associated with a memory cell phenotype, whereas cells from non-responders showed upregulation of genes linked to an effector or exhausted phenotype.[36] Since the clinical success and persistence of CAR T-cell therapy are strongly associated with the dominance of the central memory phenotype, numerous strategies have been explored to increase the proportion of central memory T cells in CAR T-cell products (reviewed in Ref.[37]).

Building on the growing evidence supporting the importance of the T_{CM} phenotype for antitumor efficacy, we evaluated whether our top-ranked elastic microstructure (0.5-4-0.5) more effectively promoted T_{CM} activation compared to *Dynabeads*™-based activation. T_{CM} cells are phenotypically characterized by the expression of CD45RO, CCR7, and CD62L.[38] To assess this, we subjected PBMCs from three healthy donors to a CAR T-cell production protocol using activation via antibody-coated 0.5-4-0.5 surfaces. As controls, we used flat PDMS surfaces (0.5 GPa)

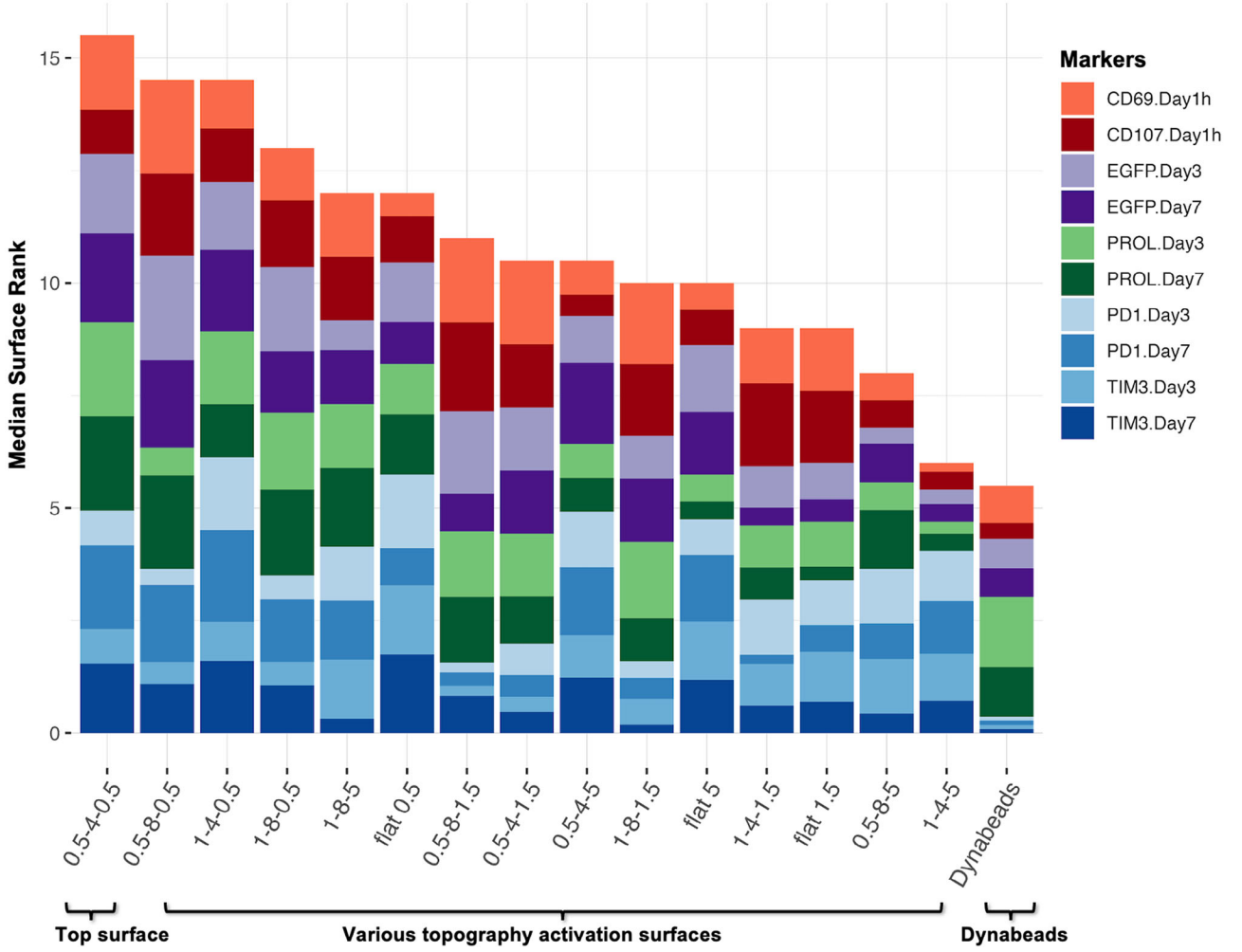

Figure 2. Visualization of the relative performance of all activation surfaces based on the median rank of performance for each feature. The features represent spanning various aspects of surface activity, including Activation markers (CD69 and CD107), Exhaustion markers (PD1 and TIM3), Proliferation (PROL), and Transduction (EGFP). Each marker is also specified by the relevant time points (Day 1, 3, or 7), which are accounted for as distinct features of surface activity. For each surface topology, the height of the bar represents the overall rank across all features, while the relative contribution of each feature to the total bar height is indicated by its corresponding color segment. Note that we computed the overall surface rank with Activation, Proliferation, and Transduction markers positively correlated with performance (higher values are better) and Exhaustion markers (PD1 and TIM3) as negatively correlated with performance (lower is better). Surface "0.5-4-0.5" achieved the highest ranking across all features, whereas Dynabeads showed the lowest ranking compared to antibody-coated surfaces. Note that control flat surfaces (0.5 or 1.5 or 5) without coating antibodies ranked at the bottommost and for clarity are not shown in the graph.

and antibody-coated *Dynabeads*™. We analyzed CD45RO and CCR7 expression on $CD3^+$ T cells before activation (designated as day 0, see **Figures** 3a,b and S13, Supporting Information for the gating strategy) and on days 3 and 7 of the protocol (Figure 3c–f). Initially, the majority of $CD3^+$ T cells displayed either a $CD45RO^-CCR7^+$ (naïve) or $CD45RO^+CCR7^-$ (effector) phenotype.

Activation by all three tested surfaces substantially increased the $CD45RO^+CCR7^+$ fraction on days 3 and 7, with similar enhancements observed for flat PDMS and *Dynabeads*™ (Figure 3c–f). However, the 0.5-4-0.5 surface significantly amplified this fraction, nearly doubling its levels compared to the increases already induced by flat PDMS and *Dynabeads*™. This enhancement was consistent across all three donors. The T_{CM} fraction continued to increase on day 7 compared to day 3 for all activation methods. Additionally, we investigated whether the enhanced central memory phenotype on day 7 was associated with transduction efficiency. The vector used for viral transduction on day 2 encoded both the CAR and EGFP. Both CAR-transduced (Figure 3g,h) and non-transduced (Figure 3i,j) $CD3^+$ T cells (EGFP-positive and EGFP-negative, respectively) displayed similar CD45RO and CCR7 staining patterns, indicating that successful transduction with CAR-encoding lentiviruses on day 2 was not specifically associated with the central memory phenotype.

5. 3D Elastic Microstructures Boost CAR-T Cell's Effector Function

Next, we investigated whether T-cell stimulation on elastic microtopography prior to CAR transduction influences the

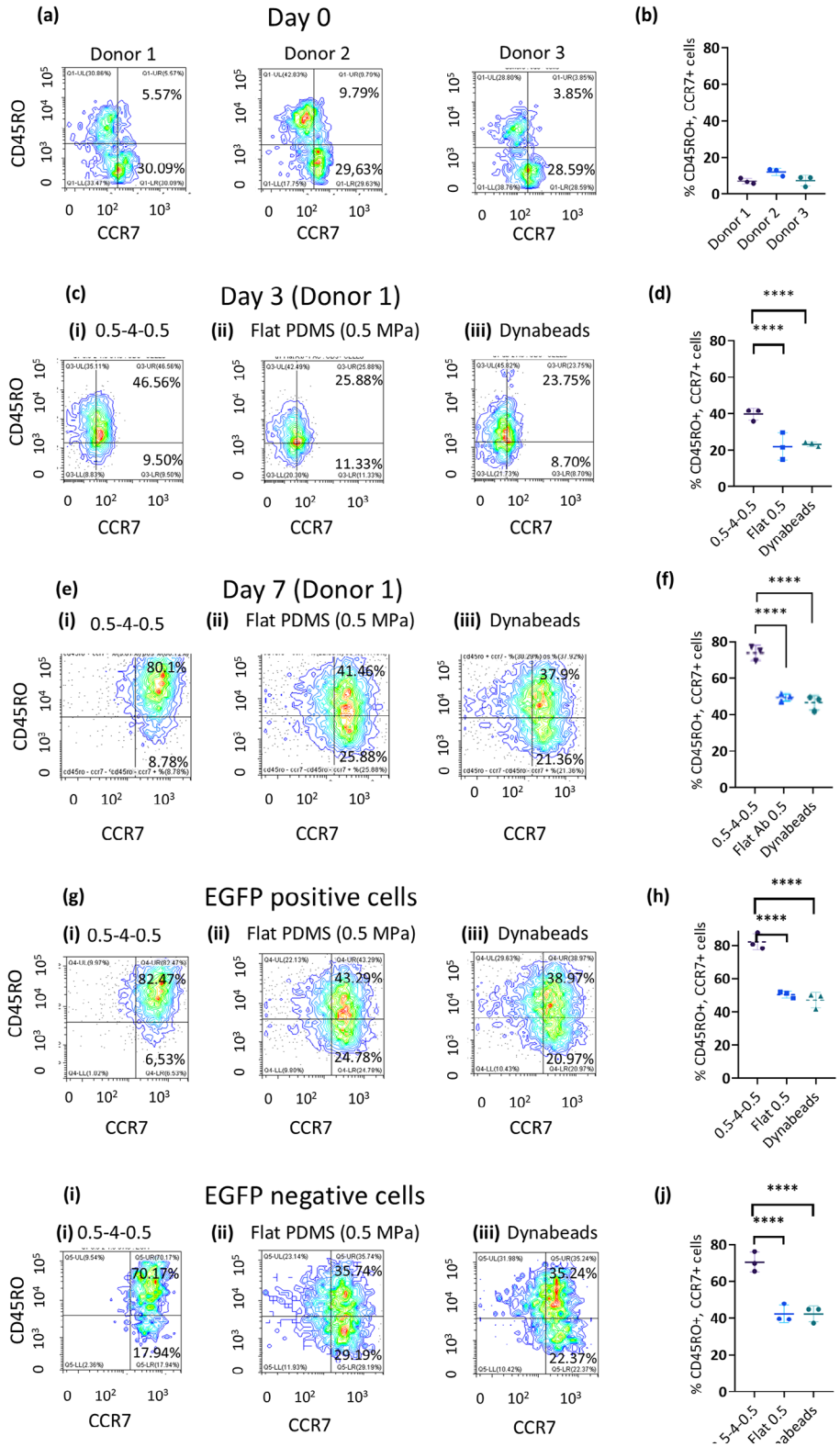

Figure 3. Differentiation of CAR-T cells into central memory type upon activation with various stimuli. a) Representative flow cytometry plots for analyzing the phenotype of activated CAR-T cells. Peripheral blood mononuclear cells (PBMCs) were gated, followed by gating for single cells and exclusion of dead cells (DAPI negative). $CD3^+$ T cells were then gated and further analyzed for CD45RO and CCR7 expression at Day 0 before activation. b) Graph represents the percentage of $CD45RO^{++}$ $CCR7^{++}$ cells among $CD3^+$ T cells at Day 0 for Donor 1, 2, and 3. c,e) depict flow cytometry gating strategy for analyzing CD45RO and CCR7 expression at Day 3 and Day 7 respectively after activation for Donor 1. d,f) graphs represent the percentage of $CD45RO^+$

functional response of the resulting CAR T cells against target cancer cells. To this end, PBMCs from three donors were activated using antibody-coated elastic microstructures (0.5-4-0.5), with antibody-coated flat PDMS (0.5 MPa) and *Dynabeads*™ as controls, followed by transduction with anti-HER2 CAR.[39] After more than seven days of culture, CAR T-cell function was assessed through co-incubation with HER2-positive JIMT-1 target cells, a human breast ductal adenocarcinoma cell line (**Figure 4a**). Lysis of JIMT-1 cells was significantly higher for T cells activated on the 0.5-4-0.5 surface compared to those activated on flat PDMS or *Dynabeads*™, at both 1:1 and 3:1 CAR T-cell-to-cancer-cell ratios (Figure 4b,c).

Additionally, we used the Immuno-Tumor ex vivo Assay (iTEVA) assay to evaluate HER2-directed CAR T-cell function on 3D tumor explants derived from HER2-positive PDX models[40,41] (Figure 4d). IFNγ secretion from T cells activated on the 0.5-4-0.5 surface and incubated with HER2-positive 3D explants was significantly higher compared to those activated on flat PDMS or *Dynabeads*™ (Figure 4e). Ki-67 expression in sections from 3D explants co-cultured with 0.5-4-0.5 activated T cells was significantly lower than in those co-cultured with flat PDMS-activated T cells and similar to those activated with *Dynabeads*™ (Figure 4f). These results collectively demonstrate that HER2-directed CAR T cells activated using the 0.5-4-0.5 elastic microstructure exhibited superior effector function compared to activation with either flat PDMS or *Dynabeads*™. To confirm that the observed differences in T-cell responses to different surfaces were not due to variations in antibody coverage, we examined antibody distribution across different stiffnesses and topographies (Figure S14, Supporting Information). Importantly, the antibody coverage of PDMS samples with a 0.5 MPa modulus—including both flat and 0.5-4-0.5 micropillar surfaces—as well as 0.5-4-1.5 and 0.5-4-5, was equivalent to that of *Dynabeads*™. This confirms that the superior performance of the 0.5-4-0.5 surface over *Dynabeads*™ and flat PDMS was not attributable to differences in antibody coverage.

6. In Vivo Assessment of CAR-T Cell Effector Function

To further investigate the benefits of T-cell stimulation on elastic topographic surfaces, we evaluated the in vivo potency of HER2-directed CAR T cells produced using activation on the 0.5-4-0.5 surface, flat PDMS, and *Dynabeads*™ (all antibody-coated). NSG mice were inoculated with 10^6 and 2×10^6 luciferase-expressing JIMT-1 cells into the left and right flanks, respectively. Tumor progression was monitored using intraperitoneal injection of the bioluminescent reporter luciferin, followed by measurement of its intensity. CDXs were allowed to grow for two weeks, reaching similar average sizes across all experimental groups. On day 7, cultured HER2-directed CAR T cells (5×10^6 per mouse) were injected intravenously, and tumor size was monitored on days 1, 4, 7, and 11 after CAR T-cell treatment (**Figure 5a** presents measurements from all tumor-bearing mice at each post-treatment time point). The experiment was terminated 30 days after JIMT-1 inoculation, at which point blood samples were collected to assess the percentage of remaining human $CD3^+$ and $CD3^+CD8^+$ T cells in circulating PBMCs.

By day 11, CDX growth was significantly suppressed in mice treated with CAR T cells activated on the 0.5-4-0.5 surface compared to all other experimental groups (Figure 5b). Specifically, tumor growth in the 0.5-4-0.5-treated group was significantly lower than in the negative control group. In contrast, there was no statistically significant difference between *Dynabeads*™-treated mice and the negative control. Additionally, the percentage of circulating human $CD3^+$ T cells was highest in the 0.5-4-0.5-treated group compared to controls, whereas the lowest $CD3^+$ percentage was observed in the *Dynabeads*™-activated CAR T-cell-treated group (Figure 5c.i). The fraction of $CD8^+$ cells within the circulating human $CD3^+$ population was also significantly higher in the 0.5-4-0.5-treated group than in both flat PDMS- and *Dynabeads*™-activated groups (Figure 5c. ii).

Further analysis of T-cell activation and central memory markers revealed that CD69 and CD45RO expression were significantly higher in human T cells (both $CD3^+$ and the $CD8^+$ subset) retrieved from the 0.5-4-0.5-treated group compared to the other groups. While CCR7 expression levels were similar across groups, they were slightly higher in the 0.5-4-0.5 group (Figure 5d,e). This result aligns with the CAR T-cell state prior to inoculation: a substantial fraction of cells in the flat PDMS- or *Dynabeads*™-activated groups that were not $CD45RO^+CCR7^+$ still expressed CCR7 (Figure 3). The similar CCR7 expression across groups may indicate the presence of naïve T cells rather than T_{CM} cells in the circulating CAR T cells from the flat PDMS- and *Dynabeads*™-activated groups.

6.1. The Activation with 3D Elastic Microstructures Results in a Transcriptional Signature of Central Memory T Cells

To further explore whether the observed CAR T cell response is associated with T cell phenotype directed by the stimulating surface, we performed whole-transcriptome profiling of peripheral blood mononuclear cells (PBMCs) across four donors and three Ab-coated activation surfaces 0.5-4-0.5 surface, flat PDMS (0.5 MP), and Dynabeads (**Figure 6a**). We performed RNA sequencing, standard quality control, and transcriptional quantification (see Methods), followed by the analysis to identify Differentially Expressed Genes (DEGs) and differentially represented cells and cell states on our selected topography. Notwithstanding the high levels of variation among donors, we observed

$CCR7^+$ cells among $CD3^+$ T cells activated with 0.5-4-0.5 elastic microstructure, Dynabeads, and FLAT antibody over three days and seven-days period respectively for Donor 1, Donor 2, and Donor 3. g,i) depict representative flow cytometry plots used to assess CD45RO and CCR7 expression at Day 7 post-activation, distinguishing between EGFP positive and EGFP negative cells respectively for Donor 1. h,j) graphs illustrate the percentage of $CD45RO^+$ $CCR7^+$ cells within EGFP positive and EGFP negative T cell subsets respectively, after seven days of activation with various stimuli (0.5-4-0.5 elastic microstructure, Dynabeads, and FLAT antibody). The data encompasses three donors: Donor 1, Donor 2, and Donor 3. Error bars represent standard deviation. Asterisks denote significant differences ($^*p \leq 0.05$, $^{**}p \leq 0.01$, $^{***}p \leq 0.001$, $^{****}p \leq 0.0001$) determined by one-way ANOVA analysis using GraphPad Prism.

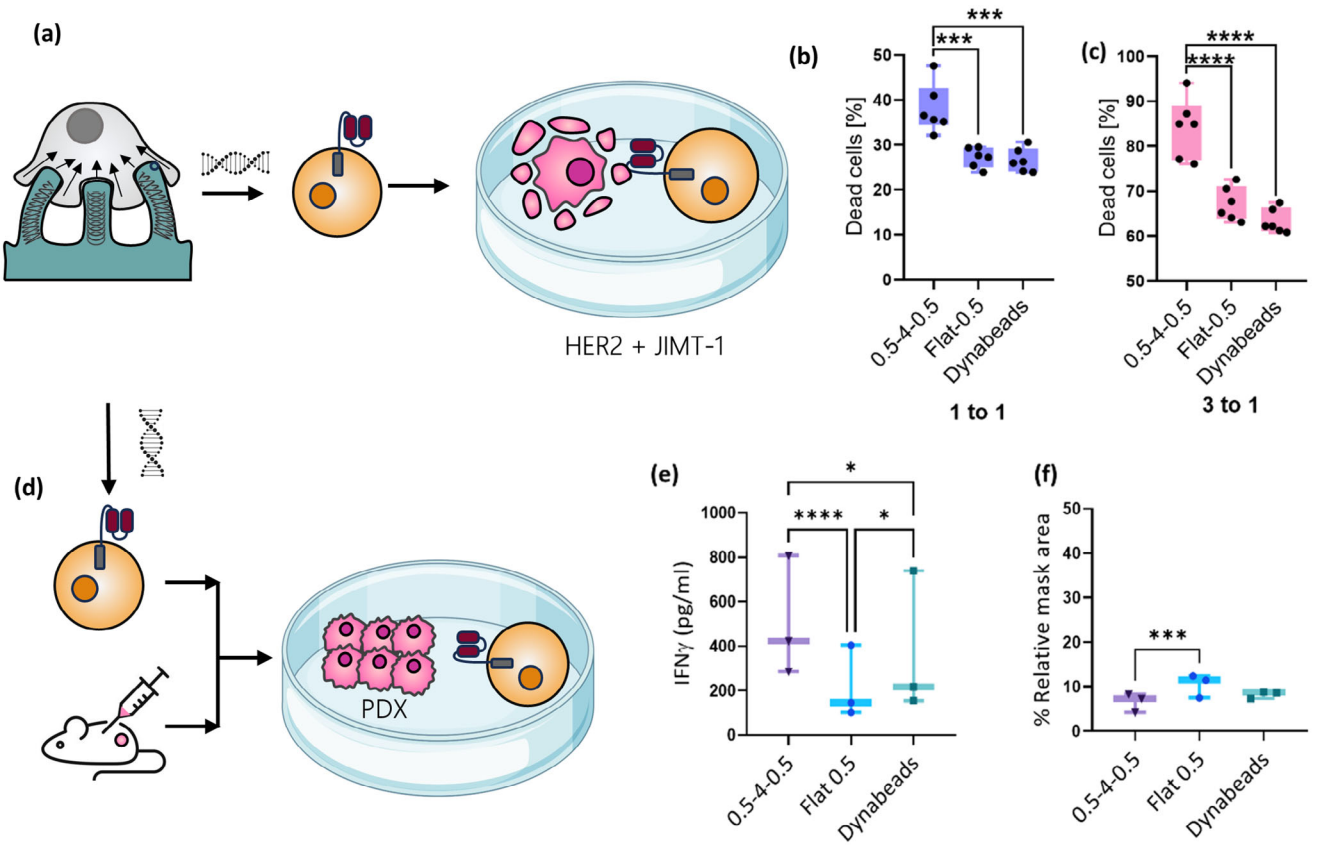

Figure 4. Functional activity of HER2-directed CAR-T cells activated with various stimuli. a) The schematic diagram for activation, CAR transduction and culture protocol, and functional assay either with cell line target or with 3D explant. b,c) Killing of JIMT-1 target cells by HER2-directed CAR-T cells activated on day 1 with the different surfaces and assessed for killing activity following day 7 of culture (summary of 3 different CAR-T donors), for 1:1 and 3:1 CAR T cell: cancer cell ratios, respectively. d) iTEVA ex vivo assay to test the function of the CAR-T cells. HER2-positive PDX was implanted subcutaneously in the dorsal flank of immune-deficient mice. After reaching a size of 500 mm^3, PDX was harvested and sectioned into $2 \times 2 \times 2$ mm^3 3D-tumor explants that were plated in 96 well plates (one explant per well) and incubated with 20000 CAR-T cells for 18 h. e) INFγ secretion to the supernatant in the well was measured by ELISA, a summary of 3 different CAR-T donors. f) Following the 18 h incubation with the CAR-T cells, tissue microarray blocks were prepared from the $2 \times 2 \times 2$ 3D-explants, and Ki-67 expression was analyzed by staining of 5µ sections (termed as %relative mask area in y-axis). A high relative mask area indicates a high proliferation rate of the tumor tissue. One-way ANOVA was performed using GraphPad Prism. Bars represent the standard deviation, and asterisks represent significant differences ($p \leq 0.05^{*}$, $p \leq 0.01^{**}$, $p \leq 0.001^{***}$, $p \leq 0.0001^{****}$).

significant DEGs when comparing the transcriptional profiles of T cells when activated to our chosen topography (0.5-4-0.5) compared with Dynabeads, with CD27 and GZMB with the highest statistical significance among the genes that are overexpressed (Figure 6b). In the Supporting Information, we describe DEGs for the 0.5-4-0.5 surface compared with that of the flat surface. Next, we focused on the characterization of the transcriptional state of T cells. To that end, we performed Gene Set Enrichment Analysis (GSEA, see Experimental Section and Supporting Tables) with the reference transcriptional signatures in the Monaco database.[42] For T cells activated on the 0.5-4-0.5 surfaces, we observed enrichment in several immune states including various T cells and T helper subtypes. Additionally, we observed a pronounced enrichment in the transcriptional signatures of T CD8, T CD8 Memory, and specifically, T CD8 Central-Memory (CM) with Normalized Enrichment Scores (NES) of 2.18, 1.87, and 2.02, respectively (Figure 6c,d). Interestingly, the central memory signatures were predominantly driven by TRBV (T-cell receptor Beta Variable) and TRAV (T-Cell Receptor Alpha Variable), as visualized in Figure 6D. These TRAV and TRBV genes play crucial roles in the diversity and specificity of the T-cell receptor (TCR) repertoire.

6.2. Activation with 3D Elastic Microstructures Reduces T Cell Toxicity Following Electroporation-Based Gene Transfection

Gammaretroviral- and lentiviral-based gene delivery are leading strategies for CAR-T cell generation. However, due to variable transduction efficiency, high cost, and the risk of insertional oncogenesis with retroviral-based methods, non-viral alternatives are extensively explored.[43–46] Electroporation – the leading non-viral method, offers high efficiency, however, it is accompanied by toxicity to transfected PBMCs.[47,48] Here, we aimed to compare our novel activating surface and standardly used T cell activating platform – Dynabeads, in terms of their effects on the electroporation efficiency and toxicity.

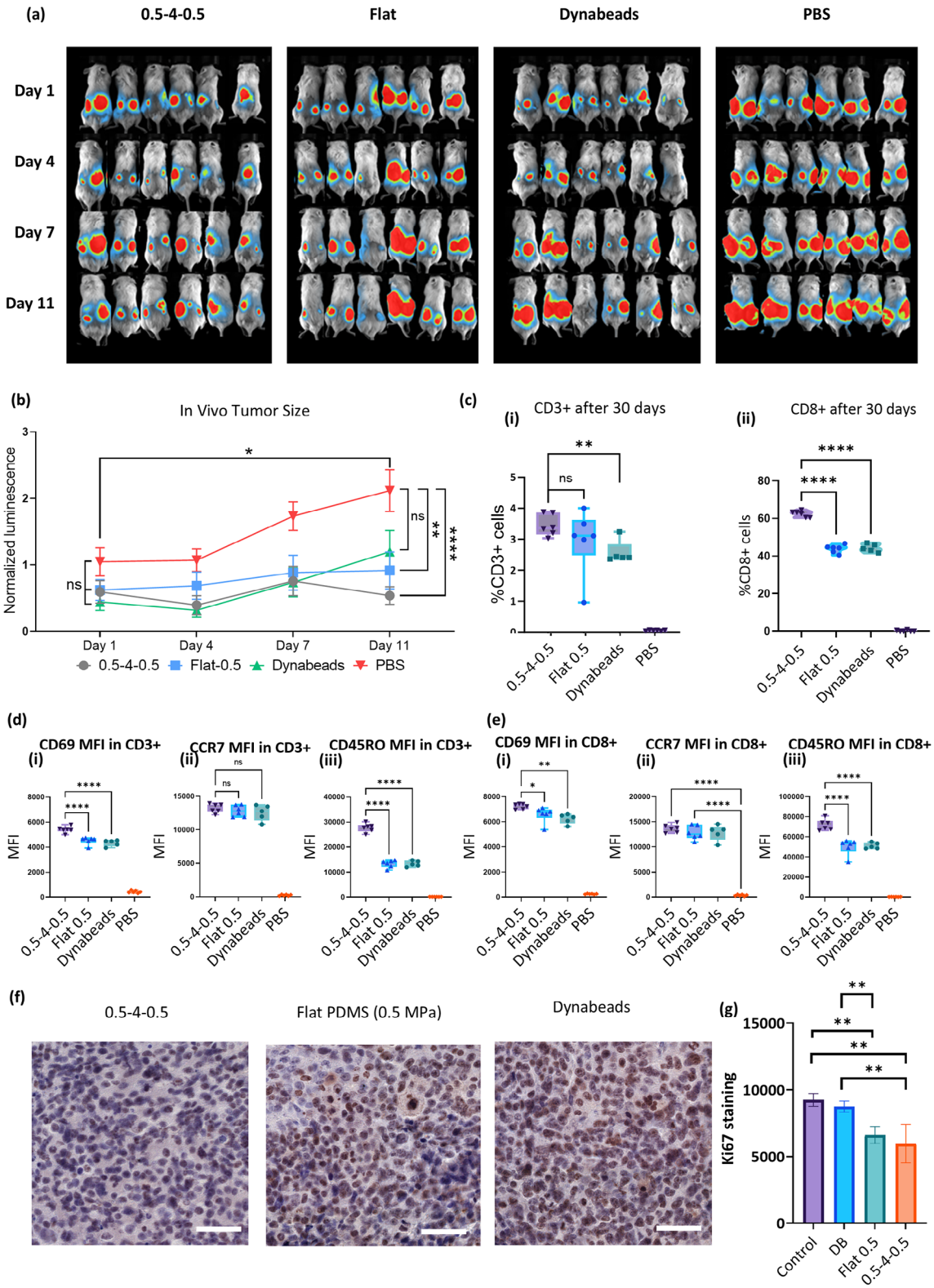

Figure 5. Functional Assessment of CAR-T Cells via in vivo studies. a) Luciferase expressing JIMT1 cells were subcutaneously injected into the dorsal flank of NSG mice. After two weeks, mice were divided into four treatment groups: PBS, Dynabeads, Flat antibody, and 0.5-4-0.5. These groups received intravenous administration of PBS (1X) as control or pre-activated CAR-T cells using Dynabeads or Flat antibody or 0.5-4-0.5 microstructure surface. Tumor progression was monitored on Day 1, 4, 7, and 11 post-treatment using luciferin reporter. b) The graph illustrates the normalized intensity of bioluminescence for each treatment group on Days 1, 4, 7, and 11, depicting tumor response to CAR-T cell therapy. For each mouse, for all days,

Prior to electroporation, one million pre-activated PBMCs were plated in 100 µL of OptiMEM™ within an electroporation cuvette. The PBMCs were pre-activated using Dynabeads, 0.5-4-0.5 PDMS surface, and control flat PDMS with no antibodies (named as flat no A.B). Notably, Dynabeads-conjugated PBMCs underwent additional magnet isolation to purify the cell population before electroporation, as Dynabeads might interfere during electroporation. The presence of Dynabeads in the cell population could be toxic for cells during electroporation because it has the potential to interference or have adverse effects on cell integrity during subsequent electroporation.[47] Cell viability and insertion efficacy post-electroporation were compared between Dynabeads-conjugated and PDMS surface-activated PBMCs. Both protein-based (Cas9-eGFP) and DNA-based (eGFP-encoding DNA vector) electroporation were assessed. Electroporation efficiency was evaluated by flow cytometry after 2 h for Cas9 tagged eGFP protein and 24 h later for double-stranded eGFP encoding DNA vector. The cells were stained with DAPI and PE anti-human-CD3 for flow cytometric analysis. Live cell percentage was high (>90% DAPI negative) and similar between 0.5-4-0.5-activated PBMCs electroporated with either dsDNA or eGFP-tagged Cas9 protein as compared to non-electroporated PBMCs. Yet, Dynabeads-activated PBMCs reduced viability to ≈60% following gene electroporation (Figure S15a, Supporting Information). As expected, PDMS-based activation but without coated antiCD3/antiCD28 antibodies resulted in no specific activation and thus reduced the viability of PBMCs. For both protein-based or gene-based transfection, efficiency following electroporation was significantly higher in 0.5-4-0.5 activated PBMCs as compared to Dynabeads-activated and PDMS without antibodies-based activation (Figure S15b, Supporting Information).

7. Discussion

In this study, we engineered a T-cell activating platform with rationally designed elasticity and nanoscale topography. Broadly, materials and miniaturized structures with controlled mechanical properties can be used for T-cell activation to serve two primary purposes. The first is to mimic the natural mechanical cues encountered by T cells, thereby enabling the investigation of how these cues influence T-cell signaling and response.[49–51] The second is to create optimal activation conditions for achieving desired functional outcomes, even when the material properties do not necessarily mimic those of target or antigen-presenting cells.[11,52] In this context, materials with controlled elasticity and microtopography have shown promise as antibody-carrying platforms for efficient T-cell activation, with potential future applications in T-cell priming for immunotherapy.[10] However, their impact on the final outcome—namely, the antitumor efficacy of the produced T cells—remains largely unexplored. While previous studies have primarily examined the effects of these materials on signaling and activation, activation alone, though essential, is only one component of effective immunotherapeutic T-cell priming. For instance, excessive activation can lead to hypofunction and exhaustion, which in turn can negatively impact CAR transduction and antitumor efficacy. Therefore, the design of the stimulatory environment—including its topography and mechanical properties—must be carefully controlled to sustain both CAR transduction and antitumor potency. The effects of these parameters should be evaluated at each stage of immunotherapeutic cell production to optimize in vivo antitumor efficiency.

In this work, we optimized the topography and elasticity of the activating platform based on a series of critical T cell outcomes—activation, exhaustion, proliferation, and transduction efficiency. Notably, for some of these outcomes, relatively high within-donor variability was observed in cells activated by PDMS pillars, compared, for instance, to cells activated by Dynabeads™. The reasons for this variability remain unclear. A control experiment examining the uniformity of antibody coating was conducted, and its result eliminated coating inconsistencies as a possible factor (S16). Still, despite the differing variabilities in the basic outcomes used for the initial screening, T cells produced using 0.5-4-0.5 surface and Dynabeads™ exhibited similar variability in subsequent functional assays evaluating the generation of T_{CM} cells and cancer killing.

Guiding CAR T-cell differentiation toward the central memory (T_{CM}) subset rather than a terminally differentiated state is crucial for effective tumor killing, as demonstrated in this study and other recent works.[28,29,53,54] However, the exact mechanism by which activation on elastic microstructures enhances the T_{CM} subset remains to be elucidated. Several non-mutually exclusive possibilities must be considered: i) Preferential activation of the T_{CM} subset within the PBMCs isolated from the donor's blood. ii) A significantly higher proliferation rate of T_{CM} cells during CAR T-cell culturing compared to other T-cell subsets, such as naïve or terminally differentiated T cells,[55,56] and iii) Gradual upregulation of CCR7 and CD45RO on the cell membrane during CAR T-cell culture, leading to an increased proportion of cells expressing these T_{CM} markers.[57,58] Despite these open questions, the consistent increase in the T_{CM} subset across different donors suggests that tuning the physical conditions of T-cell priming—such as the elasticity and morphology of the antibody-carrying surface—is a promising strategy for enhancing CAR T-cell therapy efficacy.

The mechanism by which the mechanical properties of the stimulating surface influence T-cell activation is intriguing yet remains largely unexplored. In general, T cells exert

integrated intensity in ROIs (two per mouse, left and right flank) was depicted and normalized to the average of the PBS control group on day one. c) Flow cytometry analysis of peripheral blood mononuclear cells (PBMCs) collected on Day 30 post-treatment- PBMCs were stained for different cell markers. The flow cytometry gating strategy involved gating for PBMCs, single cells, and exclusion of dead cells. $CD3^+$ T cells (c.i) were further analyzed for $CD8^+$ T cell (c.ii) subsets. $CD3^+$ (d) and $CD8^+$ e) T cells were gated separately for expression of CD69 (d. i and e.i), CCR7 (d.ii and e.ii), and CD45RO (d.iii and e.iii) markers. Toward the end of the experiment, tumor samples were surgically removed and then processed for hematoxylin and Ki67 staining. f) Representative images of control and treated groups showing the expression of proliferation marker Ki-67. Ki-67 positive cells are visualized as brown staining. Magnification = 40X, bars = 50 µm. (g) Bars histogram of object frequency of Ki67. A high % of relative mask area indicates a high proliferation rate of the tumor tissue. Error bars represent standard deviation, and asterisks denote significant differences ($^*p \leq 0.05$, $^{**}p \leq 0.01$, $^{***}p \leq 0.001$, $^{****}p \leq 0.0001$) determined by the Wilcoxson non-parametric test or by one-way ANOVA test using GraphPad Prism.

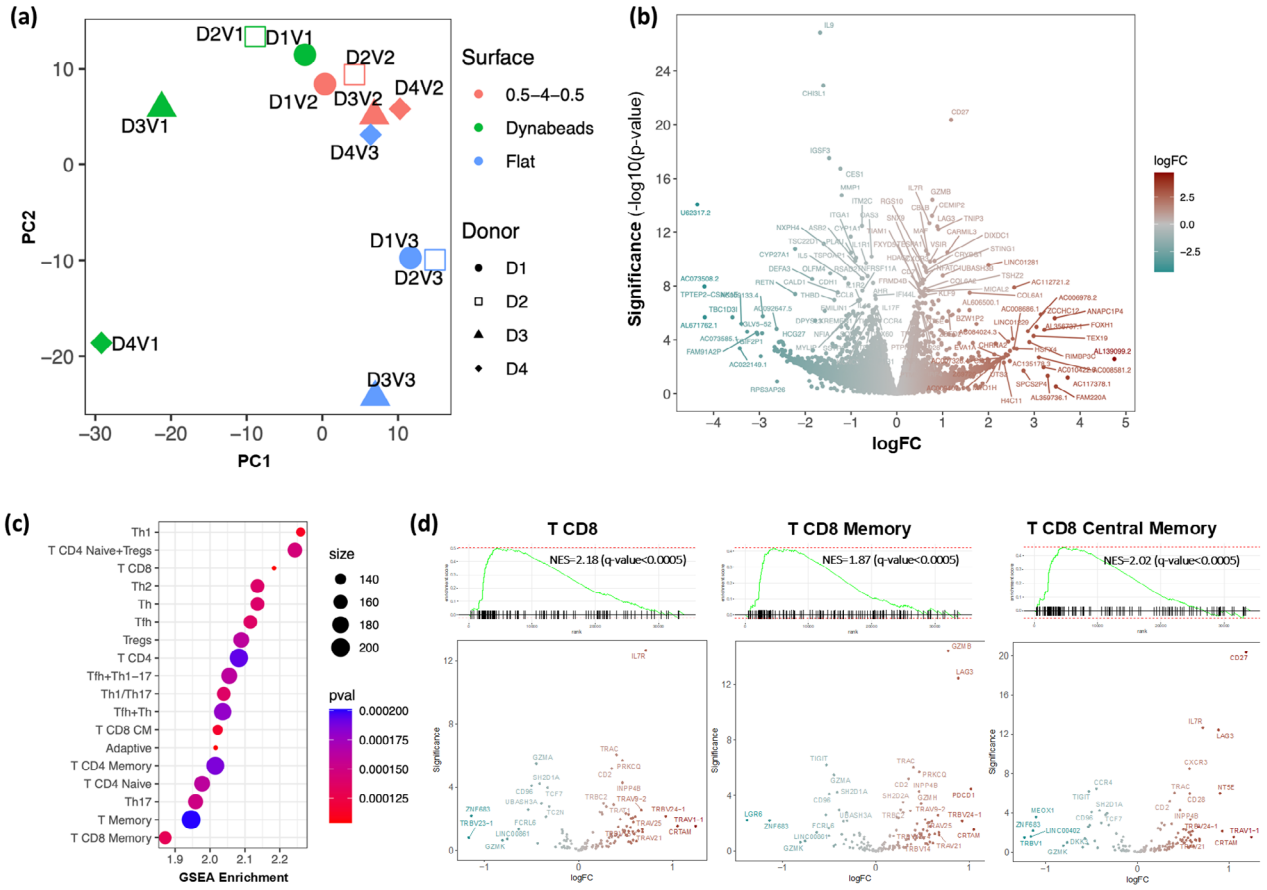

Figure 6. RNA-seq analysis of immune states activation surfaces treatment. a) Principal Component Analysis (PCA) dimensionality reduction of whole-transcriptome profiles for 12 samples spanning three surface treatments (Optimized, Dynabeads, and Flat) and four human donors. b) Visualization of DEGs comparing treatment with Optimized surface and Dynabeads as a Volcano Plot (gene over-expressed in our optimized surface area with positive log-fold-change, logFC). c) Depiction of the top enriched gene signatures in the Monaco Immune-states data d) Gene set enrichment and Gene set-specific Volcano plots depicting the significantly enriched signature of T CD8, T CD8 Memory, and specifically, T CD8 Central-Memory (CM) following our optimized surface treatment.

contractile forces when engaging target surfaces, driven by retrograde actin flow, which is essential for the formation of the immune synapse. Previous studies have shown that soft activating surfaces facilitate the formation of small protrusions through which T cells probe surface mechanical properties.[50] These protrusions, in turn, generate localized membrane deformations that induce spatial segregation between the TCR and CD45, thereby modulating TCR signaling.[5,59] The geometry of the pillar used in this work was chosen to induce membrane curvature similar to that induced by the naturally formed protrusions. Also, the materials used in our activating surfaces had elasticities ranging from 0.5 to 5 MPa—well above the physiological elasticity range of T-cell environments, which typically spans from a few hundred pascals to ≈100 kPa. However, when assessing the mechanical response of the surface to cellular forces, it is essential to consider its microstructure. Specifically, T cells primarily interact with and apply forces to the tips of the micropillars, which deflect like flexible cantilevers. As a result, the dense micropillar array generates a mechanical response that depends not only on the material's bulk elasticity but also on its microstructural geometry. In our previous work, we used finite element analysis to demonstrate that a micropillar array made of PDMS with an elasticity of 1 MPa produces a collective mechanical resistance to T-cell forces equivalent to that of a flat surface that is five orders of magnitude softer.[60] This resistance is similar to that of the natural mechanical environment of T cells, including target and antigen presenting T cells. Therefore, microstructuring the ex vivo activating surface with pillars makes it as close as possible, mechanically, to the in vivo "activating surfaces". However, the impact of the micropillars on T-cell activation is not solely due to their "effective softening" of the activating surface. The microtopography itself induces localized membrane deformations, whose role in T-cell activation remains largely unexplored. The spatial segregation between engaged TCRs and large phosphatases, driven by membrane curvature induced by the microtopography, is likely one of the factors regulating T-cell activation and subsequent functional responses.[15,61] Yet, further study is needed to verify this hypothesis.

The ease of fabricating surfaces with controlled elasticity and topography for T-cell activation greatly facilitates their potential clinical implementation. These surfaces can be produced in a scalable manner and integrated into both manual protocols and

automated bioreactors for CAR T-cell production. For instance, we recently reported a scalable, self-assembly-based fabrication method for such nanostructures.[62] Here, we employed this approach to produce a 90 mm circular surface with 0.5-4-0.5 pillars, which fit the bottom of a sufficiently large petri dish for stimulating 50 million PBMCs. The stimulation resulted in activation and proliferation levels comparable to those observed with the smaller-area samples described earlier (Figure S17, Supporting Information). PDMS was selected as the base material due to its widespread use in biomedical applications and full compatibility with GMP standards, including standard sterilization methods.[63] However, other biocompatible polymers with similar properties should also be explored. Notably, within the tested stiffness range, PDMS exhibits purely elastic behavior, meaning that elasticity was the only material property examined. In contrast, the physiological T-cell activating environment is viscoelastic, and the effect of the viscous component (i.e., creep and stress relaxation) of the activating material on T-cell responses has only recently been investigated.[64] Based on our findings, we anticipate that future innovations will integrate both elastic and viscous mechanical elements to optimize the efficient and cost-effective production of CAR T cells for potent immunotherapies.

8. Experimental Section

Fabrication of PDMS Surfaces with Topographies: The surfaces were fabricated based on the previous report,[60] using double replication from Silicon master molds containing pillars of different geometries produced by electron beam lithography and plasma etching. Anti-sticking coating was based on trichloro(1*H*,1*H*,2*H*,2*H*-perfluorooctyl) silane was deposited on Silicon Master molds overnight in a vacuum. The negative replica was produced by pouring the standard Sylgard 184 PDMS kit mixture (10:1 PDMS/hardener) on the master mold, curing for an hour at 60 °C, peeled off, and subsequently coating with an anti-adhesive layer of trichloro(1*H*,1*H*,2*H*,2*H*-perfluorooctyl)silane. The pillar containing PDMS surfaces were similarly produced from the replicas, by pouring the mixtures PDMS: hardener in the corresponding ratios, curing for an hour at 60 °C, and peeling off. To obtain PDMS with the elastic moduli, of 0.5, 1.5, and 5 MPa, the ratios of 1:20, 1:10, and 1:5, respectively, were used.

PDMS Biofunctionalization: PDMS samples were functionalized with antibodies as previously described[60] wherein surfaces were functionalized with a mix of activating ligands α-CD3 and α-CD28. Briefly, the samples were first treated in a UV ozone cleaner for 5 min and immediately functionalized with (3-aminopropyl)triethoxysilane (APTES, Sigma-Aldrich) by immersing in a 5% ethanolic APTES solution for 30 min, rinsing thrice with ethanol, and baking for 30 min in an oven at 60 °C. Following the APTES step, samples were sterilized in 70% ethanol for 1 h, and all subsequent steps were performed in a sterile laminar flow. The samples were incubated overnight at 4 °C in a 2 µg mL^{-1} solution of 1:1 v/v of anti-human CD3 (OKT3 clone, Biolegend) and anti-human CD28 (Biolegend) in sterile phosphate-buffered saline (PBS), then rinsed three times, and stored in sterile PBS until their use, no less than 1 h after.

PBMC Isolation and Activation: PBMCs were isolated from fresh blood samples that were taken from adult volunteers as approved by the Helsinki Ethics Committee (approval no. 0062-23-SOR). Using a DG-vein set (VSET21), 14 mL of peripheral blood was drawn into an LH Lithium Heparin tube (Greiner Bio-One, Austria, Kremsmünster) from healthy, willing donors. The blood was placed into an Amersham Bioscience Ficoll-paqueTM plus, diluted 1:1 with 1X PBS, and centrifuged at 1200 g for 30 min to separate the components. Following interphase collection, cells were activated for 24 h. Activation with Dynabeads™ human T-Activator CD3/CD28 (Cat. No. 11131D, ThermoFisher): cells were mixed with the Dynabeads according to the manufacturer's recommendation (1:1 bead to cell ratio). Then, 600000 mixed cells/well were plated on 48-well plates in 0.6 mL Nutri-T medium (Cat. No. 05-F3F2111-1K, Sartorius-Beit Haemek) supplemented with 200 IU ml^{-1} of rhIL2 (Cat. No. 200-02-500UG, Pepro-Tech, Cranbury, NJ, USA). Activation with the various surfaces: surfaces were placed in 48-well plates and then coated-functionalized with 100 ng mL^{-1} of anti-human CD3 (OKT3) and 100 ng mL^{-1} of anti-human CD28 (Cat No. 317347 and 302902, respectively, BioLegend, San Diego, USA). Following the washing of functionalized surfaces with ethanol and PBS, 600000 cells/well were plated in in 0.6 mL Nutri-T supplemented with rIL-2 as above. Note that the Nutri-T medium was also supplemented 1 mM Sodium pyruvate, 2 mM L-glutamine, 10 mM Hepes, 0.1 mM NEAA (all from Sartourious-Beit Haemek), and 1% Pen Strep (Gibco, MA, USA).

Transduction in T cells: After 24 h of activation with either Dynabeads or the various surfaces, PBMCs were washed twice with 1X PBS, gently detached from the activating surfaces, and transferred to a new sterile 48-well plate after washing twice with 1X PBS. The cells were sedimented by centrifuging at 500 g for 5 min at room temperature. For transduction, in 48 well plates, 600 µL of 600000 cells were infected with 400 µL of lentivirus containing anti-HER2 3rd generation CAR supplemented with 200 IU ml^{-1} of rIL2and 6 nM of BX795 (Cat. No. #tlrl-bx7, InVivoGen). Note that the lentiviral vector also encoded for eGFP, eGFP encoding sequence was connected to the CAR encoding sequence through the T2A sequence, used to transduced cells were in direct correlation. The cells were incubated at 37 °C with 5% CO_2 for 24 h, and the cells were washed twice with 1X PBS to remove cell-free virus and BX795. The cells were then maintained in Nutri-T medium with 200 IU ml^{-1} of rIL2.

Electroporation: To evaluate the effect PBMC activation on transfection efficiency by electroporation, 1 million PBMCs were suspended in 100 µL of OptiMEM™ (Gibco) were added in the electroporation cuvette (Nepa electroporation cuvettes, 2 mm). For Dynabeads, magnets were used to remove the beads before performing electroporation. Cas9 tagged with eGFP protein (170 µg per 1×10^6 cells) or 2 µg of double-stranded eGFP DNA was added to the cuvettes. Electroporation was performed by Super Electroporator Nepa 21 type 2 (NepaGene™) according to the manufacturer's instructions. The electroporation settings were as follows: poring pulse: 175 V, pulse time 3.5 ms, pulse interval 50 ms, with 2 pulses and decay rate of 10, transfer pulse: 20 V, pulse time 50 ms, pulse interval 50 ms, with 5 pulses and decay rate of 40. After electroporation, the cells were seeded to 1 mL of Nutri-T in 24 well plate. The electroporation efficiency was analyzed by flow cytometer after 2 h for Cas9 tagged eGFP and 24 h later for double stranded eGFP. The cells were stained with 1 µg/ml DAPI (Cat No. 422801, BioLegend)and 1 µg ml^{-1} PE-conjugated anti-human-CD3 (UCHT1) (Cat. No. 300441, Biolegend, San Diego, CA) for the flow cytometry.

Flow cytometry: For flow cytometry measurements, 50 000 cells were used per well. The cells were washed with 1X PAF (PBS-0.05% Sodium Azide-2% FCS) and seeded in 96 well plates. The cells were then stained with respective fluorophore-conjugated antibodies as specified in the table, in 1:100 dilution (1 µg ml^{-1} concentration) and incubated for 30 min on ice. Thereafter, the cells were washed, and the dead cells were stained with DAPI (1 µ ml^{-1}). All the samples were analyzed in Beckman CytoFLEX LX flow cytometer. For analysis, the fraction of CD3-positive cells was calculated, and CD3-positive cells were then analyzed for staining with the other antibodies employed for staining.

Degranulation: For degranulation, 50 000 CAR-T cells/well and PCP-C5.5-conjugated anti-human CD107a (Cat. No. 328616, Biolegend, San Diego, CA) were added to 150000 JIMT1 cells/well in a 96-well plate. The cells were kept at 37 °C, 5% CO_2 for 4 h. The cells were stained again with PCP-C5.5-conjugated anti-human CD107a for 30 min on ice after being washed. The dead cells were stained with 1ug ml^{-1} of DAPI followed by flow cytometric analysis.

Effect of the Activated PBMC on Patient-Derived Xenografts: To evaluate the effect of the cells activated by PDMS, patient-derived xenografts were incubated in the presence of the pre-activated PBMCs, and the immunologic response in the form of interferon-gamma secretion was measured. Following Helsinki Ethics Committee approval, tumor biopsy sample LSE19 was collected from the Soroka Medical Center and implanted subcutaneously in the dorsal flank of immune-deficient NOD scid gamma

(NSG) mice (approved by Ben-Gurion University Committee for the Ethical Case and Use of Animals in Experiments, authorization number IL56-06-2023E). The animals were housed in standard microisolator cages with a 12-h light cycle and food and water. The tumor size was monitored periodically every 2–3 days using a digital caliper by measuring the length and width of the tumor. Animals were monitored for weight loss every 3 days. After the xenografts reached the size of over 1000 mm^3, they were excised and sectioned into $2 \times 2 \times 2$ mm^3 tumor explants and immune-tumor-ex vivo-assay (iTEVA) was performed as follows. The explants were incubated in 48 well flat bottom plates for 18–20 h with either 20000 or 50000 PBMCs activated on either flat PDMS surfaces, Dynabeads, 1-2-5, or 0.5-2-1.5 PDMS micro-structures. The incubation was performed in NutriT media supplemented with 1 mM sodium pyruvate, 2 mM L-glutamine, 0.1 mM MEM nonessential amino acids, 1% penicillin/streptomycin, 10 mM HEPES (Life Technologies, Waltham, MA, USA), 30 IU of IL-2 (200-02-500UG, PeproTech, Cranbury, NJ, USA). After the incubation, the supernatant from the wells was collected and subjected to analysis using a standard IFN-γ ELISA assay (BioLegend, San Diego, CA, USA). The tumor explants were subjected to IHC and Ki67 assays and analysis.

In Vivo Luciferase Assay: 6–8-week-old female NSG mice were injected subcutaneously with JIMT1-luc-puro (1×10^6 cells on the right flank and 2×10^6 cells on the left flank). On Day 7, 3 mg per mice of luciferin was injected intraperitoneally and imaged under IVIS Imaging System (A2S Vilber Newton 7.0) and software (Kuant). Mice were randomized based on tumor radiance before CAR-T cell injection. On the same day 1×10^7 CAR-T cells were injected intravenously through the tail along with 2 mg per mice of IL-15 injected intraperitoneally. The tumors were analyzed in IVIS Imaging System on Day 4, Day 7, and Day 11 after CAR-T cell injection. On the same days of analysis, IL-15 was injected. After the experiment, the mice were sacrificed, and blood was collected for PBMCs extraction. The tumors were also excised and FFPE blocks were prepared.

Formalin-Fixed Paraffin Embedded (FFPE) Block Preparation and Tissue Microarray Construction: The process of FFPE blocks and construction of tissue microarrays (TMAs) involved several steps. Initially, an automated tissue processing machinery (Leica Biosystems, Nubloch, Germany) was utilized to create FFPE blocks from the tumor tissue explants. Subsequently, using 3-mm T-SueTM punch needles (Simport, Beloeil, QC, Canada), TMA blocks were prepared from the donor FFPE blocks, each containing a maximum of 24 tissue explants. The paraffin-embedded tissue TMA blocks were then sectioned into 5 µm slices using a microtome.

Immunohistochemical Staining, Image Analysis, and Quantification: Following TMA construction, immunohistochemical staining, image analysis, and quantification were performed. The tissue sections underwent deparaffinization using xylene, followed by antigen retrieval through heat treatment in citrate buffer (pH 6). To inhibit endogenous peroxidase activity, a 3% hydrogen peroxide (H2O2) solution was applied, followed by blocking with a solution containing phosphate-buffered saline (PBS) with 0.1% Tween and 5% bovine serum albumin (BSA). Primary antibodies, such as the Ki67 anti-human primary antibody (Merck, Ref- 275R-14) diluted to 1:200, were then incubated with the sections overnight at 4 °C. Subsequently, an IHC ABC kit (VECTASTAIN Cat. VE-PK-6200, VectorLabs) was utilized for color detection, followed by counterstaining with hematoxylin (Cat. 1051750500, Merck) to visualize cellular nuclei. Finally, the stained cells were mounted using VectaMount® permanent mounting medium (REF- H-5000, VectorLabs), and high-resolution digital images of the slides were captured using a Pannoramic Scanner (3DHISTECH, Budapest, Hungary). The scanned images were then analyzed using Pannoramic Viewer software to assess and quantify immunohistochemical staining patterns.

Statistical Analysis: For Figure 2 and Figures S4–S10 and Table S1 (Supporting Information) the activation potency of all surfaces was quantified and compared it to Dynabeads, across ten features, including Activation markers (CD69 and CD107) on Day 1, Exhaustion markers (PD1 and TIM3) on Days 3 and 7, Proliferation (PROL), Days 3 and 7, and Transduction (EGFP). First, the differences among surfaces were assessed using raw data measurement of the three replicates for each of the ten features and across each of the three donors. Analysis of Variance (ANOVA) was performed to compare the mean activity levels across surfaces. The Benjamini–Hochberg method was applied to control the False Discovery Rate (FDR), resulting in q. values for multiple-test hypothesis correction (Table S1, Supporting Information). To aggregate the measurements across donors, a Z-score was calculated to normalize the measurements and alleviate the donor-specific variability. The Z-score value of zero was defined by Dynabeads value per donor (i.e., specified for each donor: D1, D2, D3) by subtraction of the mean value of Dynabeads measurements. Furthermore, the values were scaled by dividing by the standard deviation of the measurements across all surfaces for each outcome to normalize for donor-specific variability. To rank the surfaces by each "feature" (marker by time-point), the median score for each of the ten features was computed, including Activation markers (CD69 and CD107) on Day 1, Exhaustion markers (PD1 and TIM3) on Days 3 and 7, Proliferation (PROL), Days 3 and 7, and Transduction (EGFP), at Days 3 and 7 where the Z-score values of 9 measurements were accounted for (three donors in three replicates, see FiguresS4–S9, Supporting Information). To obtain an inclusive score for surface topologies while accounting for all features, the surface topologies were ranked based on their median rank among all ten features (Figure 2, Figure S10, Supporting Information). The overall surface rank was computed, with Activation, Proliferation, and Transduction markers positively correlated with performance (higher values are better) and Exhaustion markers (PD1 and TIM3) negatively correlated with performance (lower is better). The top surface ("0.5-4-0.5") had the highest median and mean rank, accounting for all features. A two-sided Welch's Two Sample *t*-test was then performed, without assuming equal variances, to compare the top surface ("0.5-4-0.5") to Dynabeads with the 9 z-scored measurements, spanning 3 donors, each with 3 replicates and used FDR corrected q. values as described above (Table S2, Supporting Information). Data presentation for Figure 2 was a stacked bar chart, and for Figures S4–S9 (Supporting Information) was boxplot with dots (thus, sample size can be observed). Statistical analyses were performed using the R programming language (version 4.2.3). Note that Tukey's honestly significant difference (HSD) post-hoc test was applied after omnibus ANOVA to compare activation levels between Dynabeads and each of the 15 antibody-coated activation surfaces (legend to Table S1, Supporting Information).

For Figures 3–5 and Figure S15 (Supporting Information): Statistical analysis was performed with GraphPad Prism 8. Data for bar graphs was presented either as mean ± SD (Figure 3 and Figure 5g) or as a boxplot (Figures 4 and 5, Figure S14, Supporting Information). The sample size for bar graphs is between 3 and 9. The significance of the data presented was determined by one-way analysis of variance (ANOVA), and probabilities were two-sided. This use of ANOVA was equivalent to a *t*-test, thus, post-hoc tests for pair-wise comparisons are not applicable. Note that for Figure 5b (Tumor size over time as measured by luminescence), a sample size of 10 (5 mice x 2 tumors) and the statistical assay used was the Wilcoxson non-parametric test. Differences were considered to be statistically significant at a two-sided $P < 0.05$.

For Figure 6: The statistical analysis of RNA-seq was described in detail in the Supporting Information. For data presented as Volcano plots (Figure 6b,d), differentially Expressed Genes (DEG) analysis was performed using reads while accounting for the among-donors batch effect. FDR for multiple-test hypotheses was used to correct p-values for DEGs and for the data presented as Gene Set Enrichment Analysis (GSEA, Figure 6c). Statistical analyses were performed using the R programming language (version 4.2.3).

Supporting Information

Supporting Information is available from the Wiley Online Library or from the author.

Acknowledgements

A.A-K.Y. and C.U.M. equally contributed to this work. Funding: Israel Innovation Authority, (IAA, Project 84927, M.S. and A.P.); United States-Israel

Binational Science Foundation (BSF, Project 2023087 to A.P.); Cooperation Program in Cancer Research of the Deutsche Krebsforschungszentrum (DKFZ) and Israeli; Ministry of Science, Technology and Space (MOST) (DKFZ-MOST, Project 0006605 to A.P.); Deutsche Forschungsgemeinschaft, Middle East Program, (DFG, Project SM 289/10-1. 488 to M.S.); Israel Science Foundation (ISF, Project 2016/21 to M.S.); Israeli Ministry of Science Technology and Space (MOST, Project 5912 to O.C.); Israel Science Foundation (ISF, Project 2802/22 to O.C.); Ofiice of the Assistant Secretary of Defense for Health Affairs through the Peer Reviewed Cancer Research Program (Project W81XWH-20-1-0417 to S.G.). [Correction added on June 20, 2025, after first online publication: Acknowledgement Section has been updated.]

Conflict of Interest

The authors declare no conflict of interest.

Data Availability Statement

Research data are not shared.

Keywords

biomaterials, CAR T cells, immunotherapy, mechanosensing

Received: August 22, 2024
Revised: April 29, 2025
Published online: May 9, 2025

[1] S. A. Grupp, M. Kalos, D. Barrett, R. Aplenc, D. L. Porter, S. R. Rheingold, D. T. Teachey, A. Chew, B. Hauck, J. F. Wright, M. C. Milon, B. L. Levine, C. J. June, *N. Engl. J. Med.* **2013**, *368*, 1509.
[2] C. H. June, R. S. O'Connor, O. U. Kawalekar, S. M. Ghassemi, *Science* **2018**, *359*, 1361.
[3] S. Ghassemi, S. Nunez-Cruz, R. S. O'Connor, J. A. Fraietta, P. R. Patel, J. Scholler, D. M. Barrett, S. M. Lundh, M. M. Davis, F. Bedoya, C. Zhang, J. Leferovich, S. F. Lacey, B. L. Levine, S. A. Grupp, C. H. June, J. J. Melenhorst, M. C. Milone, *Cancer Immunol. Res.* **2018**, *6*, 1100.
[4] S. Ghassemi, J. S. Durgin, S. Nunez-Cruz, J. Patel, J. Leferovich, M. Pinzone, F. Shen, K. D. Cummins, G. Plesa, V. A. Cantu, S. Reddy, F. D. Bushman, S. I. Gill, U. O'Doherty, R. S. O'Connor, M. C. Milone, *Nat. Biomed. Eng.* **2022**, *6*, 118.
[5] S. J. Davis, P. A. van der Merwe, *Nat. Immunol.* **2006**, *7*, 803.
[6] S. Minguet, M. Swamy, B. Alarcón, I. F. Luescher, W. W. A. Schamel, *Immunity* **2007**, *26*, 43.
[7] M. Huse, *Nat. Rev. Immunol.* **2017**, *17*, 679.
[8] R. Basu, B. M. Whitlock, J. Husson, A. Le Floc'h, W. Jin, A. Oyler-Yaniv, F. Dotiwala, G. Giannone, C. Hivroz, N. Biais, J. Lieberman, L. C. Kam, M. Huse, *Cell* **2016**, *165*, 100.
[9] J. Husson, K. Chemin, A. Bohineust, C. Hivroz, N. T. Henry, *PLoS One* **2011**, *6*, 19680.
[10] W. Jin, F. Tamzalit, P. K. Chaudhuri, C. T. Black, M. Huse, L. C. T. Kam, *Proc. Natl. Acad. Sci. USA* **2019**, *116*, 19835.
[11] R. S. O'Connor, X. Hao, K. Shen, K. Bashour, T. Akimova, W. W. Hancock, L. C. Kam, M. C. Milone, *J. Immunol.* **2012**, *189*, 1330.
[12] Y. Razvag, Y. Neve-Oz, J. Sajman, M. Reches, E. Sherman, *Nat. Commun.* **2018**, *9*, 732.
[13] Y. Jung, L. Wen, A. Altman, K. Ley, *Nat. Commun.* **2021**, *12*, 3872
[14] Y. Jung, I. Riven, S. W. Feigelson, E. Kartvelishvily, K. Tohya, M. Miyasaka, R. Alon, G. Haran, *Proc. Natl. Acad. Sci* **2016**, *113*, E5916.
[15] M. Aramesh, D. Stoycheva, I. Sandu, S. J. Ihle, T. Zünd, J.-Y. Shiu, C. Forró, M. Asghari, M. Bernero, S. Lickert, M. Kotowski, S. J. Davis, A. Oxenius, V. Vogel, E. Klotzsch, *Proc. Natl. Acad. Sci* **2021**, *118*, 2107535118.
[16] B. Han, Y. Song, J. Park, J. Doh, *J. Controlled Release* **2022**, *343*, 379.
[17] A. S. Cheung, D. K. Y. Zhang, S. T. Koshy, D. J. Mooney, *Nat. Publ. Group* **2018**, *36*, 160.
[18] H. Wang, D. J. Mooney, *Nat. Mater.* **2018**, *17*, 761.
[19] J. Hyun, S. J. Kim, S.-D. Cho, H.-W. Kim, *Biomaterials* **2023**, *297*, 122101.
[20] L. H. Lambert, G. K. E. Goebrecht, S. E. De Leo, R. S. O'Connor, S. Nunez-Cruz, T. D. Li, J. Yuan, M. C. Milone, L. C. Kam, *Nano Lett.* **2017**, *17*, 821.
[21] A. D. Posey, R. M. Young, C. H. June, *Trends Cancer* **2024**, *10*, 687.
[22] J. L. Tan, J. Tien, D. M. Pirone, D. S. Gray, K. Bhadriraju, C. S. Chen, *Proc. Natl. Acad. Sci. USA* **2003**, *100*, 1484.
[23] N. Q. Balaban, U. S. Schwarz, D. Riveline, P. Goichberg, G. Tzur, I. Sabanay, D. Mahalu, S. Safran, A. Bershadsky, L. Addadi, B. Geiger, *Nat. Cell Biol.* **2001**, *3*, 466.
[24] O. du Roure, A. Saez, A. Buguin, R. H. Austin, P. Chavrier, P. Silberzan, B. Ladoux, *Proc Nat Acad Sci USA* **2005**, *102*, 2390.
[25] F. Tamzalit, M. S. Wang, W. Jin, V. Boyko, J. M. Heddleston, C. T. Black, L. C. Kam, M. I. Huse, *Sci. Immunol.* **2019**, *5445*, 443309.
[26] A. Wahl, C. Dinet, P. Dillard, A. Nassereddine, P.-H. Puech, L. Limozin, K. Sengupta, *Proc. Natl. Acad. Sci. USA* **2019**, *116*, 5908.
[27] X. Yin, L. He, Z. Guo, *Immunology* **2023**, *169*, 400.
[28] C. S. Hinrichs, Z. A. Borman, L. Gattinoni, Z. Yu, W. R. Burns, J. Huang, C. A. Klebanoff, L. A. Johnson, S. P. Kerkar, S. Yang, P. Muranski, D. C. Palmer, C. D. Scott, R. A. Morgan, P. F. Robbins, S. A. Rosenberg, N. P. Restifo, *Blood* **2011**, *117*, 808.
[29] P. Graef, V. R. Buchholz, C. Stemberger, M. Flossdorf, L. Henkel, M. Schiemann, I. Drexler, T. Höfer, S. R. Riddell, D. H. Busch, *Immunity* **2014**, *41*, 116.
[30] L. Gattinoni, E. Lugli, Y. Ji, Z. Pos, C. M. Paulos, M. F. Quigley, J. R. Almeida, E. Gostick, Z. Yu, C. Carpenito, E. Wang, D. C. Douek, D. A. Price, C. H. June, F. M. Marincola, M. Roederer, N. P. Restifo, *Nat. Med.* **2011**, *17*, 1290.
[31] G. D. Trobridge, R. A. Wu, M. Hansen, C. Ironside, K. L. Watts, P. Olsen, B. C. Beard, H.-P. Kiem, *Mol. Ther. J. Am. Soc. Gene Ther.* **2010**, *18*, 725.
[32] M. Schmueck-Henneresse, B. Omer, T. Shum, H. Tashiro, M. Mamonkin, N. Lapteva, S. Sharma, L. Rollins, G. Dotti, P. Reinke, H.-D. Volk, C. M. Rooney, *J. Immunol. Baltim. Md* **1950**, *199*, 348.
[33] L. Liu, E. Bi, X. Ma, W. Xiong, J. Qian, L. Ye, P. Su, Q. Wang, L. Xiao, M. Yang, Y. Lu, Q. Yi, *Nat. Commun.* **2020**, *11*, 5902.
[34] J. A. Fraietta, C. L. Nobles, M. A. Sammons, S. Lundh, S. A. Carty, T. J. Reich, A. P. Cogdill, J. J. D. Morrissette, J. E. DeNizio, S. Reddy, Y. Hwang, M. Gohil, I. Kulikovskaya, F. Nazimuddin, M. Gupta, F. Chen, J. K. Everett, K. A. Alexander, E. Lin-Shiao, M. H. Gee, X. Liu, R. M. Young, D. Ambrose, Y. Wang, J. Xu, M. S. Jordan, K. T. Marcucci, B. L. Levine, K. C. Garcia, Y. Zhao, et al., *Nature* **2018**, *558*, 307.
[35] S. M. Collins, K. A. Alexander, S. Lundh, A. J. Dimitri, Z. Zhang, C. R. Good, J. A. Fraietta, S. L. Berger, *Sci. Adv.* **2023**, *9*, adh2605.
[36] G. López-Cantillo, C. Urueña, B. A. Camacho, C. Ramírez-Segura, *Front. Immunol.* **2022**, *13*, 878209.
[37] S. K. Ghorai, A. N. Pearson, *Cureus* **2024**, *16*, 65291.
[38] S. Yang, L. Gattinoni, F. Liu, Y. Ji, Z. Yu, N. P. Restifo, S. A. Rosenberg, R. A. Morgan, *Cancer Immunol. Immunother. CII* **2011**, *60*, 739.
[39] Y. Greenshpan, O. Sharabi, A. Ottolenghi, A. Cahana, K. Kundu, K. M. Yegodayev, M. Elkabets, R. Gazit, A. Porgador, *Commun. Biol.* **2021**, *4*, 1.
[40] R. Keshet, J. S. Lee, L. Adler, M. Iraqi, Y. Ariav, L. Q. J. Lim, S. Lerner, S. Rabinovich, R. Oren, R. Katzir, H. Weiss Tishler, N. Stettner, O. Goldman, H. Landesman, S. Galai, Y. Kuperman, Y. Kuznetsov, A.

Brandis, T. Mehlman, S. Malitsky, M. Itkin, S. E. Koehler, Y. Zhao, K. Talsania, T. Shen, N. Peled, I. Ulitsky, A. Porgador, E. Ruppin, A. Erez, *Nat. Cancer* **2020**, *1*, 894.
[41] W. Shalata, M. Iraqi, B. Bhattacharya, V. Fuchs, L. C. Roisman, A. Y. Cohen, I. Massalha, A. Yakobson, M. Prasad, M. Elkabets, A. Porgador, N. Peled, *Cancers* **2021**, *13*, 3630.
[42] G. Monaco, B. Lee, W. Xu, S. Mustafah, Y. Y. Hwang, C. Carré, N. Burdin, L. Visan, M. Ceccarelli, M. Poidinger, A. Zippelius, J. Pedro de Magalhães, A. Larbi, *Cell Rep.* **2019**, *26*, 1627.
[43] H. Balke-Want, V. Keerthi, A. Cadinanos-Garai, C. Fowler, N. Gkitsas, A. K. Brown, R. Tunuguntla, M. Abou-el-Enein, S. A. Feldman, *Immuno-Oncol. Technol.* **2023**, *18*, 100375.
[44] A. Maia, M. Tarannum, R. Romee, *Stem Cells Transl. Med.* **2024**, *13*, 230.
[45] Y. Chen, M. Mach, A.-R. Shokouhi, H. Z. Yoh, D. C. Bishop, T. Murayama, K. Suu, Y. Morikawa, S. C. Barry, K. Micklethwaite, R. Elnathan, N. H. Voelcker, *Mater. Today* **2023**, *63*, 8.
[46] A.-R. Shokouhi, Y. Chen, H. Z. Yoh, J. Brenker, T. Alan, T. Murayama, K. Suu, Y. Morikawa, N. H. Voelcker, R. Elnathan, *Adv. Mater.* **2023**, *35*, 2304122.
[47] E. Harris, J. J. Elmer, *Biotechnol. Prog.* **2021**, *37*, 3066.
[48] J. Shi, Y. Ma, J. Zhu, Y. Chen, Y. Sun, Y. Yao, Z. Yang, J. Xie, *Molecules* **2018**, *23*, 3044.
[49] K. T. Bashour, A. Gondarenko, H. Chen, K. Shen, X. Liu, M. Huse, J. C. Hone, L. C. Kam, *Proc Nat Acad Sci* **2014**, *111*, 2241.
[50] M. Saitakis, S. Dogniaux, C. Goudot, N. Bufi, S. Asnacios, M. Maurin, C. Randriamampita, A. Asnacios, C. Hivroz, *eLife* **2017**, *6*, 1.
[51] E. Judokusumo, E. Tabdanov, S. Kumari, M. L. Dustin, L. C. Kam, *Biophys. J.* **2012**, *102*, L5.
[52] V. Bhingardive, A. Kossover, M. Iraqi, B. Khand, G. Le Saux, A. Porgador, M. Schvartzman, *Nano Lett.* **2021**, *21*, 4241.
[53] C. S. Hinrichs, Z. A. Borman, L. Cassard, L. Gattinoni, R. Spolski, Z. Yu, L. Sanchez-Perez, P. Muranski, S. J. Kern, C. Logun, D. C. Palmer, Y. Ji, R. N. Reger, W. J. Leonard, R. L. Danner, S. A. Rosenberg, N. P. Restifo, *Proc. Natl. Acad. Sci. USA* **2009**, *106*, 17469.
[54] C. Berger, M. C. Jensen, P. M. Lansdorp, M. Gough, C. Elliott, S. R. Riddell, *J. Clin. Invest.* **2008**, *118*, 294.
[55] S. M. Kaech, S. Hemby, E. Kersh, R. Ahmed, *Cell* **2002**, *111*, 837.
[56] E. J. Wherry, V. Teichgräber, T. C. Becker, D. Masopust, S. M. Kaech, R. Antia, U. H. von Andrian, R. Ahmed, *Nat. Immunol.* **2003**, *4*, 225.
[57] L. Yan, Y. Ou, S. Xia, J. Huang, W. Zhang, H. Shao, H. Shen, H. Bo, C. Tao, J. Wang, F. Wu, *Immunogenetics* **2022**, *74*, 231.
[58] S. Kang, L. Wang, L. Xu, R. Wang, Q. Kang, X. Gao, L. D Yu, *Oncogene* **2022**, *41*, 4696.
[59] P. A. Van Der Merwe, O. Dushek, *Nat. Rev. Immunol.* **2011**, *11*, 47.
[60] A. Pandey, M. Iraqi, E. Toledo, A. Al-Kader Yassin, E. Podvalni, S. Naaz, J. J. Pandit, C. U. Martin, G. Le Saux, A. Porgador, M. Schvartzman, *ACS Appl. Mater. Interfaces* **2023**, *15*, 31103.
[61] P. Pérez-Ferreros, K. Gaus, J. Goyette, *Front. Phys.* **2019**, *6*, 158.
[62] S. Tzadka, C. Ureña Martin, E. Toledo, A. A. K. Yassin, A. Pandey, G. Le Saux, A. Porgador, M. Schvartzman, *ACS Appl. Mater. Interfaces* **2024**, *16*, 17846.
[63] E. Briganti, T. A. Kayal, S. Kull, P. Losi, D. Spiller, S. Tonlorenzi, D. Berti, G. Soldani, *J. Mater. Sci. Mater. Med.* **2010**, *21*, 1311.
[64] K. Adu-Berchie, Y. Liu, D. K. Y. Zhang, B. R. Freedman, J. M. Brockman, K. H. Vining, B. A. Nerger, A. Garmilla, D. J. Mooney, *Nat. Biomed. Eng.* **2023**, *7*, 1374.